regime also eliminates satellite drops. This makes it possible to manufacture monodisperse gas bubbles in a viscous flow, analogous to techniques being developed to manufacture such bubbles in inertial flows (*22*). The viscous flow regime is relevant for the processing of foods, pharmaceuticals, and metal foams.

In conclusion, we observed nonuniversal, linear dynamics accompanying the formation of a smooth singularity in the breakup of a water drop in viscous silicone oil. This is the asymptotic regime for small enough values of μ_{int}/μ_{ext}, so that the interior viscosity can be neglected throughout the breakup process. For larger μ_{int}/μ_{ext}, the interior viscosity becomes important before atomic dimensions are reached. This produces a long and thin thread. The linear dynamics associated with the formation of a singularity demonstrate that there are two ways for the formation of a singularity to simplify dynamics. In the generic case, the singularity dynamics become scale-invariant, confined to a region that shrinks in all dimensions, thereby erasing all memory of boundary and initial conditions. In the case studied here, the dynamics near the singularity are characterized by an axially uniform radial collapse, so that the axial length scale remains constant, thereby making it possible for memory of the initial and boundary conditions to persist.

References and Notes

1. N. Bohr, *Nature* **143**, 330 (1939).
2. S. Chandrasekhar, *An Introduction to the Study of Stellar Structure* (Dover, New York, 1967).
3. J. Eggers, *Rev. Mod. Phys.* **69**, 865 (1997).
4. I. Cohen, S. R. Nagel, *Phys. Fluids* **13**, 3533 (2001).
5. R. E. Goldstein, A. I. Pesci, M. J. Shelley, *Phys. Rev. Lett.* **70**, 3043 (1993).
6. R. Almgren, A. L. Bertozzi, M. P. Brenner, *Phys. Fluids* **8**, 1356 (1996).
7. A. U. Chen, P. K. Notz, O. A. Basaran, *Phys. Rev. Lett.* **88**, 4501 (2002).
8. P. K. Notz, A. U. Chen, O. A. Basaran, *Phys. Fluids* **13**, 549 (2001).
9. X. D. Shi, M. P. Brenner, S. R. Nagel, *Science* **265**, 219 (1994).
10. J. D. Buckmaster, *J. Fluid Mech.* **55**, 385 (1972).
11. More precisely, it can be shown that the interior pressure $P(t)$ is given by $P(t) = \pi(\gamma/a^3) \int_{\text{drop length}} h(z, t)dz$, where a is a typical radial length scale, chosen to make the dimensionless drop volume equal to 1.
12. For nonlinear breakup dynamics, the axial curvature at the mininum κ is related to the typical axial length scale z_0 by means of $\kappa \propto h_{min}/z_0^2$. Here, $\kappa \propto 1/z_0$ because the linear breakup dynamics have no z dependence.
13. I. Cohen, M. P. Brenner, J. Eggers, S. R. Nagel, *Phys. Rev. Lett.* **83**, 1146 (1999).
14. W. W. Zhang, J. R. Lister, *Phys. Rev. Lett.* **83**, 1151 (1999).
15. A. Sierou, J. R. Lister, *J. Fluid Mech.*, in press.
16. Though we observe an approximately 100° cone for the large drop just before the breakup, the limited range of length scale over which we observe the conical profile makes it difficult to determine whether the observed cone is an asymptotic structure.
17. G. Odian, *Principles of Polymerization* (Wiley-Interscience, New York, 1991).
18. I. Cohen, H. Li, J. L. Hougland, M. Mrksich, S. R. Nagel, *Science* **292**, 265 (2001).
19. P. G. Simpkins, V. J. Kuck, *Nature* **403**, 641 (2000).
20. J. Eggers, *Phys. Rev. Lett.* **86**, 4290 (2001).
21. E. Lorenceau, F. Restagno, D. Quere, *Phys. Rev. Lett.* **91**, 184501 (2003).
22. A. M. Gañán-Calvo, J. M. Gordillo, *Phys. Rev. Lett.* **87**, 274501 (2001).

23. We thank D. Gifford for early experimental contribution to this project, and M. P. Brenner, J. Eggers, J. R. Lister, and H. A. Stone for useful discussions. Supported by the Basic Energy Sciences program of the U.S. Department of Energy (P.D. and O.A.B.); NSF grant DMR-0089081 (to I.C. and S.R.N.); NSF grant DMS-0104350 (to M.S.); and an NSF Mathematical Sciences Postdoctoral Research Fellowship (DMS-0102033), NSF grant DMR-0094569 (to L.P. Kadanoff), and the Materials Research Science and Engineering Center of NSF (to W.W.Z.).

16 July 2003; accepted 7 October 2003

A Superconducting Reversible Rectifier That Controls the Motion of Magnetic Flux Quanta

J. E. Villegas,[1] Sergey Savel'ev,[2] Franco Nori,[2,3] E. M. Gonzalez,[1] J. V. Anguita,[4] R. García,[4] J. L. Vicent[1]*

We fabricated a device that controls the motion of flux quanta in a niobium superconducting film grown on an array of nanoscale triangular pinning potentials. The controllable rectification of the vortex motion is due to the asymmetry of the fabricated magnetic pinning centers. The reversal in the direction of the vortex flow is explained by the interaction between the vortices trapped on the magnetic nanostructures and the interstitial vortices. The applied magnetic field and input current strength can tune both the polarity and magnitude of the rectified vortex flow. Our ratchet system is explained and modeled theoretically, taking the interactions between particles into consideration.

Motor proteins play a key role in the transport of materials at the cellular level (*1–3*). These biological motors are anisotropic devices that, driven by nonequilibrium fluctuations, bias the motion of particles, and which are inspiring a new generation of solid-state devices (*3–5*) that can open avenues for controlling the motion of electrons, colloidal particles, and magnetic flux quanta. Here we consider superconducting devices with anisotropic pinning, where the dc transport of magnetic flux quanta may be driven by an ac or unbiased current. Control of vortex motion with asymmetric pinning can be useful for applications in superconductivity, including field-dependent reversible vortex diodes and the removal of unwanted trapped flux from devices. Several different ways of using asymmetric pinning in superconductors to control vortex motion have been recently proposed (*6–13*). However, experiments in this area (*14*, *15*) have been difficult to control.

Earlier work on vortex dynamics in superconducting films (*16*) with regular arrays of defects (*17*, *18*), using either nonmagnetic (*19–22*) or magnetic (*23–30*) pinning traps, have explored a plethora of physical effects, including matching effects with ordered submicron magnetic defects, interstitial vortices, random versus periodic pinning, and channeling effects in the vortex lattice motion. Now that the field of vortex dynamics on periodic pinning potentials is sufficiently understood, we are in a position to take the next step of manipulating and controlling the motion of magnetic flux quanta. Preliminary numerical studies (*10*, *11*) of vortex dynamics on arrays of triangular pinning potentials have found that rectified vortex motion should occur when the system is ac-driven.

We fabricated arrays of submicron Ni triangles with electron beam lithography (*29*) on Si(100) substrates and then deposited a 100-nm-thick Nb film by dc magnetron sputtering. Several samples were fabricated with different sizes and positions of the triangles (Fig. 1A and fig. S1). For transport measurements, a cross-shaped bridge was optically lithographed and ion-etched on the Nb films (Fig. 1B, upper inset), which allowed us to inject the current either parallel (x axis) or perpendicular (y axis) to the triangular base. The Nb films grown on the array of Ni triangles showed superconducting critical temperatures between 8.3 and 8.7 K.

Magneto-transport $R(H)$ experiments, R being the resistance, were done with a magnetic field H applied perpendicular to the substrate in a liquid helium system. Fig. 1B shows the $R(H)$ data taken from the sample

[1]Departamento de Física de Materiales, Facultad Ciencias Físicas, Universidad Complutense, 28040, Madrid, Spain. [2]Frontier Research System, The Institute of Physical and Chemical Research (RIKEN), Wako-shi, Saitama, 351–0198, Japan. [3]Center for Theoretical Physics, Department of Physics, University of Michigan, Ann Arbor, MI, 48109–1120, USA. [4]Instituto de Microelectrónica de Madrid, Centro Nacional Mícroelectrónica, Consejo Superior de Investigaciones Científicas, Isaac Newton 8, Tres Cantos, 28760 Madrid, Spain.

*To whom correspondence should be addressed. E-mail: jlvicent@fis.ucm.es

with the magnetic array shown in Fig. 1A. The dc magneto-resistance exhibits commensurability effects (*24*) in which dissipation minima develop as a consequence of the geometrical matching between the vortex lattice and the underlying periodic structure. At these matching fields, the vortex-lattice motion slows down, and $R(H)$ minima appear at equally spaced values of H; $H_{match}(n) = nH_1$, with $H_1 = 32$ Oe being the first matching field and n the number of vortices per unit cell. Sharp minima in $R(H)$ were observed at the first, second, and third matching fields, but minima at higher matching fields were shallow and not well defined. The difference between the sharp and shallow minima in $R(H)$ arises because interstitial vortices appear when H is increased beyond $3H_1$. Thus, the maximum number of vortices in each triangle is three. Therefore, for each matching field, we know the number of vortices per unit cell, both inside the traps and in between them.

When an applied dc current I_{dc} is increased, the interstitial vortices depin first, producing a linear increase, in a log-log plot, of the voltage versus current (Fig. 1B, lower inset). With further increase of the applied dc current, the vortices that were initially trapped in the magnetic triangles begin to depin, producing a faster increase in $V(I_{dc})$, where V is voltage. This illustrates that there are two types of vortices subject to very different pinning energies, their motion depending on I_{dc} and H.

Fig. 2 shows what happens when, at a constant temperature T and $H = H_1 = 32$ Oe, an ac current density $J = J_{ac}\sin(\omega t)$ is injected along the x axis, where ω is the ac frequency and t is time. This yields an ac Lorentz force (F_L) on the vortices along the y axis, which is given by $\vec{F}_L = \vec{J} \times \vec{z}\phi_0$ (where $\Phi_0 = 2.07 \times 10^{-15}$ webers and $\vec{z}$ is a unit vector parallel to $\vec{H}$). Although the time-averaged force on the vortices is zero ($\langle F_L \rangle = 0$), a nonzero dc voltage drop is observed (Fig. 2, colored dots). Because the electric field $\vec{E} = \vec{B} \times \vec{v}$ ($\vec{v}$ and $\vec{B}$ being the vortex-lattice velocity and the magnetic induction, respectively), the voltage drop along the direction of the injected current probes the vortex motion along the y axis. We measured the voltage drop V_{dc} using a dc nanovoltmeter and obtained the time-averaged vortex velocity $\langle v \rangle = V_{dc}/dB$, where d is the distance between contacts and B is the magnetic induction. Thus, the vortex lattice moves on this asymmetric potential with a net velocity, as has been numerically predicted (*10*, *11*). To further test this behavior, the ac current was injected along the y axis (that is, the vortex lattice was pushed along the x axis) of the array. In this case, the dc voltage was zero (Fig. 2, black dots) because of the symmetric potential landscape along the x direction, resulting in a zero net velocity.

At a constant applied magnetic field, the dc voltage increased when the temperature decreased. At a constant temperature, increasing the applied magnetic field produced the effect shown in Fig. 3. Because we know the number of vortices in each unit cell of the array, the analysis of the experimental data is clearer for applied matching fields. The amplitude of the dc signal decreased when the magnetic field increased, because the effective pinning was suppressed by the intervortex repulsion. Moreover, when $n > 3$ (corresponding to more than three vortices per unit cell), a dc reversed signal began to develop with a maximum (Fig. 3, blue arrows) that occurred at a lower F_L than the positive-dc maxima (Fig. 3, red arrows). The interstitial vortices, which feel a weak and inverted ratchet potential, move in the opposite direction from the vortices pinned at triangles, which are subject to a strong ratchet potential. This inverse-polarity current effect was enhanced when the magnetic field was increased (Fig. 3, C to E). Finally, at very high magnetic fields, close to the normal state, a complete dc voltage reversal occurred (Fig. 3F). Measurements were performed near critical temperature (T_c) in order to make the random pinning much smaller than the triangular pinning. For slightly lower values of T, pinning became stronger and required larger applied currents to depin the trapped vortices, but the trend shown in Fig. 3 was also observed.

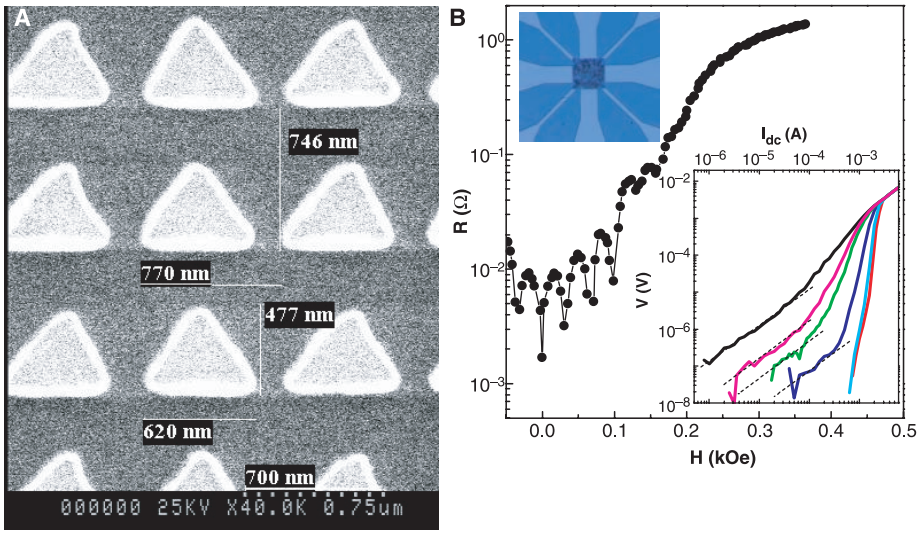

Fig. 1. (**A**) Scanning electron microscope image of an array of Ni triangles on top of Si (100) substrate. Triangle height (Ni thickness) is typically 35 nm. (**B**) dc magneto-resistance $R(H)$ in the mixed state as a function of the applied magnetic field. The temperature is $T = 0.98T_c$ and the injected dc current density is $J = 12.5$ kA·cm^{-2}. The upper inset shows a micrograph of the measuring bridge, which is 40 μm wide. The darker central area of the inset is the 90 × 90 μm^2 array of magnetic triangles. The lower inset shows voltage versus applied dc current curves at $T = 0.98T_c$. The applied magnetic fields are at the matching conditions shown by the number of vortices per unit cell: $n = 1$ (red), $n = 3$ (cyan), $n = 4$ (blue), $n = 6$ (green), $n = 8$ (magenta), and $n = 10$ (black). Dashed lines follow the ohmic behavior of the interstitials. The $V(I_{dc})$ curves change abruptly at magnetic fields from $n = 3$ to $n = 4$, because an ohmic regime appears at low currents. This is a clear signature (*21*) of the presence of interstitial vortices (vortices not pinned on the triangles).

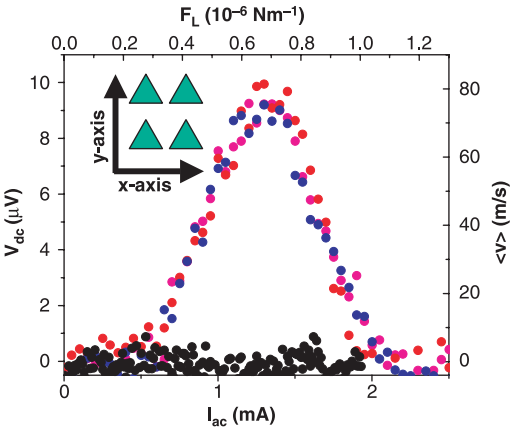

Fig. 2. dc voltage V_{dc} versus ac current density amplitude J_{ac} for an applied field $H = H_1 = 32$ Oe and $T = 0.99T_c$. V_{dc} is proportional to the net vortex-lattice velocity, $V_{dc} \propto \langle v \rangle$, whereas the Lorentz force is $F_L \propto J_{ac}$. Magenta, blue, and red circles correspond to ac frequencies $\omega = 10$ kHz, $\omega = 1$ kHz, and $\omega = 0.5$ kHz, respectively, with an ac current J injected parallel to the x axis (with F_L parallel to the y axis). Black circles correspond to $\omega = 10$ kHz, but J injected parallel to the y axis, i.e., with F_L parallel to the x axis. The inset shows the array of triangles with the x and y axes.

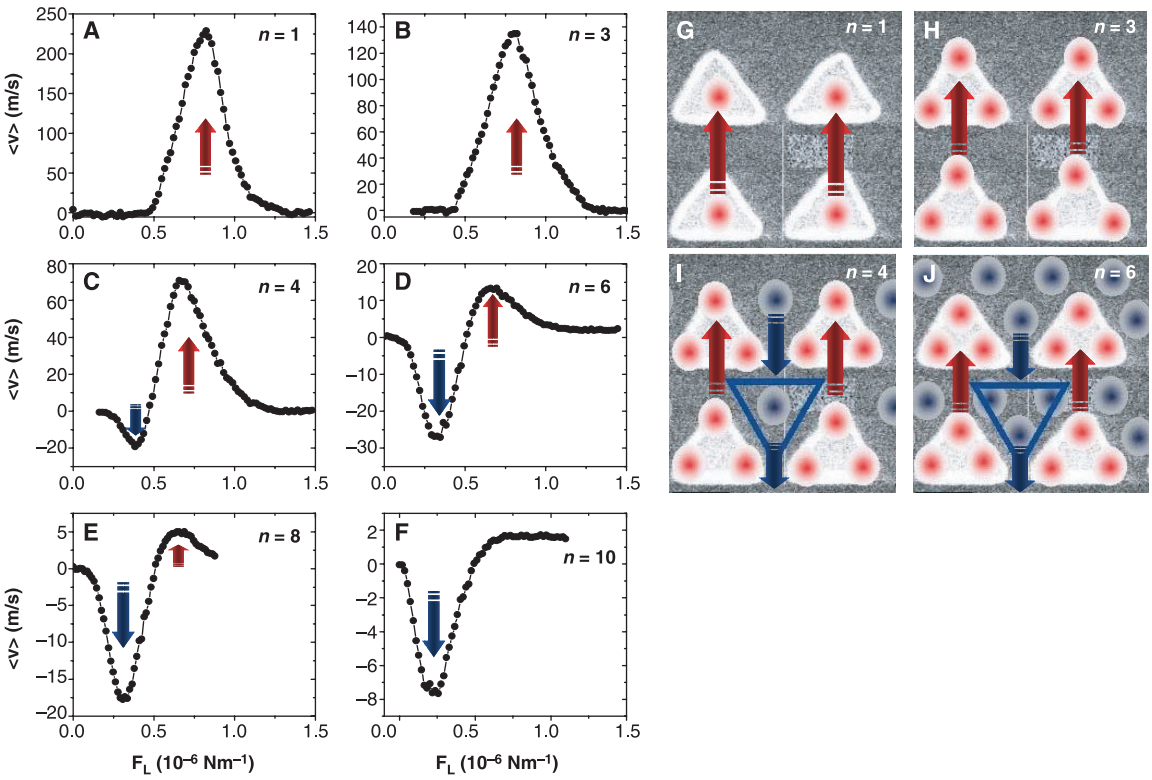

Fig. 3. (**A** to **F**) Net velocity $\langle v \rangle$ of vortices versus the ac Lorentz force amplitude (ω = 10 kHz), for several matching magnetic fields at $T = 0.98T_c$; n indicates the number of vortices per unit cell of the array. Red and black arrows show the direction of the net flow of these vortices. (**G** to **J**) Sketch of the positions of the vortices for several matching fields. Vortices pinned on the triangles are shown in red and interstitial vortices in blue.

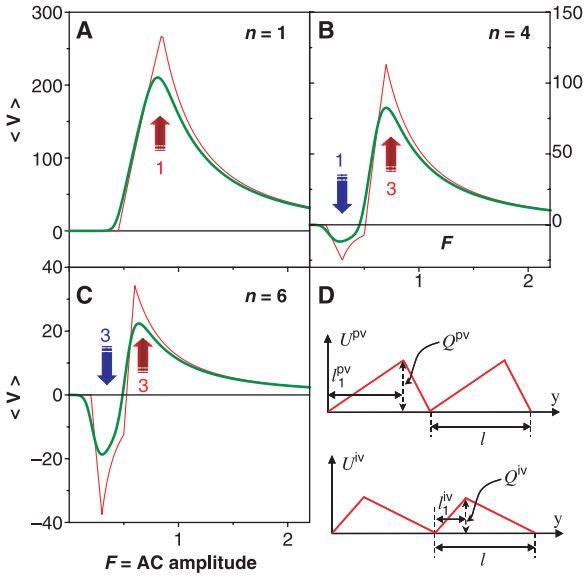

Fig. 4. (**A** to **C**) The calculated net dc velocity $\langle v \rangle$ versus ac amplitude F obtained for different effective asymmetry values $\gamma = F_{max}/F_{onset}$ with a simple model that describes the mixture of pinned and interstitial vortices. Red curves show velocities at $T = 0$ and green curves at $T/(lF_{max}) = 0.0085$, with $l = 1$ and $F_{max} = 0.85$ corresponding to pinned vortices and $n = 1$. The values of F_{max} and F_{onset} are (A) 0.85 and 0.45 for pinned vortices, (B) 0.7 and 0.5 for pinned vortices and 0.3 and 0.15 for interstitial vortices, and (C) 0.6 and 0.5 for pinned vortices and 0.3 and 0.2 for interstitial vortices. (**D**) The pinned vortices move on the asymmetric potential $U^{pv}(y)$ (top), whereas the interstitial vortices feel the potential $U^{iv}(y)$ (bottom). The latter potential is weaker, inverted, and originates from the interaction of the interstitial vortices with the pinned vortices. Here, η is taken to be 10^{-3}.

In order to interpret the experimental results, we can separate all vortices into two groups: (i) pinned vortices, which move from one triangular-shaped pinning trap to another and, thus, are directly affected by the pinning potential; and (ii) interstitial vortices, which move in between triangles and do not directly interact with the pinning traps. However, the interstitial vortices can indirectly feel the spatial asymmetry through their interactions with the pinned vortices.

This problem can be mapped onto the similar system of two species of repulsive particles (*31*), in which one type or species of particle (pinned vortices for our experiments) (Fig. 3, G to J, red dots) directly interacts with the spatially asymmetric substrate. The other type of particle (interstitial vortices) (Fig. 3, G to J, blue) is insensitive to the substrate, at least in a direct manner. It has been shown (*31*) that those particles (assigned red) subject to the substrate potential create an effective asymmetric potential, with the opposite asymmetry or opposite polarity for the other (blue) particles—if these two species repel one another. When all the particles are subjected to an ac drive force, this "inverted polarity" potential rectifies the motion of the blue particles (the interstitial vortices) in one direction. The original pinning potential rectifies the motion of the red particles (the pinned vortices) along the opposite direction, because they feel a potential with opposite polarity.

The minimal model that captures the physics of this problem can be described as follows. The pinned vortices (pv) move along the y direction on a periodic sawtooth-shaped substrate potential $U^{pv}(y) = U^{pv}(y + l)$ (Fig. 4D), where Q is the height of the potential energy barrier and l is the spatial period. With an integer m, $U^{pv}(y) = Q^{pv}(y - ml)/l_1^{pv}$ if $ml < y < ml + l_1^{pv}$, and $U^{pv}(y) = Q^{pv}[l(m + 1) - y]/(l - l_1^{pv})$ if $ml + l_1^{pv} < y < ml + l$. The interstitial vortices feel a similar but weaker potential, with the opposite polarity or opposite asymmetry, and thus have different values of Q^{iv} and l_1^{iv}, where iv is the interstitial vortices (Fig. 4D). The pinning force is sharp when vortices are being captured by or released from the islands and is comparatively weak elsewhere. However, the sharp features in the pinning forces are smoothed out by the vortex-vortex repulsive interactions and by thermal noise. To mimic anisotropy, two different slopes in the sawtooth potential are needed.

For a fixed dc external force F, the velocity $v(F,\gamma,Q)$ of the vortices on such potentials satisfies

$$v(F,\gamma,Q) = \frac{l(F - F_{c1})(F + F_{c2})}{\eta[Fl + Q\gamma - Q\gamma^{-1} + k_B T\alpha(T)]}$$

Here $\gamma = l_1/(l - l_1)$ quantifies the degree of asymmetry of the substrate; η is the viscosity; the stopping forces $\gamma F_{c1} = F_{c2} = Q(\gamma + 1)/l$ are the depinning forces to the right and to the left, respectively; k_B is the Boltzmann constant; and α is a thermal prefactor (*2*) due to thermal noise.

Now let us consider an ac driving force acting on all the vortices. In order to estimate the rectified net velocity of both the pinned and interstitial vortices, one can use the equations $\langle v^{pv}\rangle = [v(F,\gamma^{pv},Q^{pv}) + v(-F,\gamma^{pv},Q^{pv})]/2$ and $\langle v^{iv}\rangle = [v(F,\gamma^{iv},Q^{iv}) + v(-F,\gamma^{iv},Q^{iv})]/2$, respectively. The effective velocity measured in our experiments contains contributions from both the pinned vortices and the interstitial vortices. Thus, the measured velocity can be estimated as $\langle v\rangle = [\langle v^{pv}\rangle + \langle v^{iv}\rangle\beta]/(1 + \beta)$, where $\beta = n^{iv}/n^{pv}$ is the ratio of the numbers n^{pv} (shown below the red arrows in Fig. 4) and n^{iv} (above the blue arrows) of the pinned and interstitial vortices per unit cell. If the thermal noise is weak ($k_B T\alpha \approx 0$), the effective spatial anisotropy felt by the pinned and interstitial vortices can be estimated directly from the experimental data as $\gamma = F_{max}/F_{onset}$, where F_{max} is the force where the maximum of rectification occurs and F_{onset} is the force at the onset of the rectification. This simple model qualitatively describes the experimental data, even for zero thermal noise (Fig. 4, A to C, red curves). Thermal effects smooth out the calculated curves, making them much closer to the experimental results (Fig. 4, A to C, green curves). That is, the sequence of plots $\langle v\rangle(F)$ in Fig. 4 corresponds to the experimental plots in Fig. 3 and has the same qualitative trends.

Our device allows a versatile control of the motion of vortices in superconducting films. Simple modifications and extensions of it would allow the pile-up (magnetic lensing), shaping, or "sculpting" of micromagnetic profiles inside superconductors. Vortex lenses made of oppositely oriented triangles would provide a strong local increase of the vortex density at its focus regions. Thus, extensions of these types of systems could allow the motion control of flux quanta and provide a step toward devices based on the flow of magnetic flux quanta.

References and Notes

1. R. D. Astumian, *Science* **276**, 917 (1997).
2. P. Reimann, *Phys. Rep.* **361**, 57 (2002).
3. R. D. Astumian, P. Hänggi, *Phys. Today* **55**, 33 (2002).
4. H. Linke *et al*., *Science* **286**, 2314 (1999).
5. Special issue on Ratchets and Brownian Motors: Basics, Experiments and Applications, H. Linke, Ed., *Appl. Phys. A* **75** (no. 2) (2002).
6. I. Zapata, R. Bartussek, F. Sols, P. Hänggi, *Phys. Rev. Lett.* **77**, 2292 (1996).
7. J. F. Wambaugh, C. Reichhardt, C. J. Olson, F. Marchesoni, F. Nori, *Phys. Rev. Lett.* **83**, 5106 (1999).
8. C. S. Lee, B. Janko, L. Derényi, A. L. Barábasi, *Nature* **400**, 337 (1999).
9. B. Y. Zhu, F. Marchesoni, V. V. Moshchalkov, F. Nori, *Phys. Rev. B* **68**, 014514 (2003).
10. B. Y. Zhu, L. Van Look, V. V. Moshchalkov, F. Marchesoni, F. Nori, *Physica E* **18**, 322 (2003).
11. B. Y. Zhu, F. Marchesoni, F. Nori, *Physica E*, **18**, 318 (2003).
12. S. Savel'ev, F. Nori, *Nature Mater.* **1**, 179 (2003).
13. S. Weiss *et al.*, *Europhys. Lett.* **51**, 499 (2000).
14. W. K. Kwok *et al.*, *Physica C* **382**, 137 (2002).
15. R. Wördenweber, unpublished data.
16. F. Nori, *Science* **271**, 1373 (1996).
17. O. Daldini, P. Martinoli, J. L. Olsen, G. Berner, *Phys. Rev. Lett.* **32**, 218 (1974).
18. A. Pruymboom, P. H. Kes, E. van der Drift, S. Radelaar, *Phys. Rev. Lett.* **60**, 1430 (1988).
19. M. Baert, V. Metlushko, R. Jonckheere, V. V. Moshchalkov, Y. Bruynseraede, *Phys. Rev. Lett.* **74**, 3269 (1995).
20. K. Harada *et al., Science* **274**, 1167 (1996).
21. E. Rosseel *et al., Phys. Rev. B* **53**, R2983 (1996).
22. V. Metlushko *et al.*, *Phys. Rev. B* **60**, R12585 (1999).
23. Y. Otani, B. Pannetier, J. P. Nozières, D. Givord, *J. Magn. Magn. Mater.* **126**, 622 (1993).
24. J. I. Martín, M. Vélez, J. Nogués, I. K. Schuller, *Phys. Rev. Lett.* **78**, 1929 (1997).
25. D. J. Morgan, J. B. Ketterson, *Phys. Rev. Lett.* **80**, 3614 (1998).
26. J. I. Martín, M. Vélez, A. Hoffmann, I. K. Schuller, J. L. Vicent, *Phys. Rev. Lett.* **83**, 1022 (1999).
27. Y. Fasano *et al.*, *Phys. Rev. B* **60**, R15047 (1999).
28. D. Jaque, E. M. Gonzalez, J. I. Martín, J. V. Anguita, J. L. Vicent, *Appl. Phys. Lett.* **81**, 2851 (2002).
29. M. Vélez *et al.*, *Phys. Rev. B* **65**, 104511 (2002).
30. M. Vélez, D. Jaque, J. I. Martín, F. Guinea, J. L. Vicent, *Phys. Rev. B* **65**, 094509 (2002).
31. S. Savel'ev, F. Marchesoni, F. Nori, *Phys. Rev. Lett.* **91**, 010601 (2003).

32. Supported by the European Science Foundation VORTEX program, the Spanish Comision Interministerial de Ciencia y Technologia (grant no. MAT2002-04543), the Spanish R. Areces Foundation, the U.S. National Security Agency and Advanced Research and Development Activity (under Air Force Office of Scientific Research contract no. F49620-02-1-0334), the NSF (grant no. EIA-0130383), and a Ramón y Cajal contract from the Spanish Ministerio de Ciencia y Tecnología (E.M.G.).

Supporting Online Material,
www.sciencemag.org/cgi/content/full/302/5648/1188/DC1
Fig. S1

13 August 2003; accepted 9 October 2003

Stability of Peroxide-Containing Uranyl Minerals

Karrie-Ann Hughes Kubatko,[1] Katheryn B. Helean,[2] Alexandra Navrotsky,[2] Peter C. Burns[1]*

Minerals containing peroxide are limited to studtite, $(UO_2)O_2(H_2O)_4$, and metastudtite, $(UO_2)O_2(H_2O)_2$. High-temperature oxide-melt solution calorimetry and solubility measurements for studtite (standard enthalpy of formation at 298 kelvin is –2344.7 ± 4.0 kilojoules per mole from the elements) establishes that these phases are stable in peroxide-bearing environments, even at low H_2O_2 concentrations. Natural radioactivity in a uranium deposit, or the radioactivity of nuclear waste, can create sufficient H_2O_2 by alpha radiolysis of water for studtite formation. Studtite and metastudtite may be important alteration phases of nuclear waste in a geological repository and of spent fuel under any long-term storage, possibly at the expense of the commonly expected uranyl oxide hydrates and uranyl silicates.

The minerals $(UO_2)O_2(H_2O)_4$, studtite, and $(UO_2)O_2(H_2O)_2$, metastudtite, are the only known peroxide-bearing minerals. Both are readily synthesized by adding H_2O_2 to a U-bearing solution (*1*, *2*), but the conditions for their formation are uncertain. Studies of natural analogs (*3*) and many laboratory experiments (*4*–*6*) have been designed to simulate the alteration of spent fuel under conditions similar to those expected in the proposed radioactive material repository located in Yucca Mountain, Nevada, United States. These studies have emphasized uranyl oxide hydrates and uranyl silicates as dominant alteration products and have not reported the formation of uranyl peroxides. McNamara *et al.* (*7*) found studtite that had formed on the surface of spent nuclear fuel reacted at 298 K with deionized water for 1.5 years and proposed that it grew by incorporating peroxide created by the alpha radiolysis of water. Studtite is a major alteration phase associated with spent nuclear fuel contained in the K East Basins of the Hanford site, United States (*8*). Metastudtite formed on the surface of UO_2 under irradiation with a $^4He^{2+}$ (alpha-particle) beam, presumably incorporating peroxide formed by the alpha radiolysis of water (*9*). Studtite was also found on nuclear material ("lava") after the Chernobyl Nuclear Plant accident (*10*). Thus, uranyl peroxides

[1]Department of Civil Engineering and Geological Sciences, University of Notre Dame, 156 Fitzpatrick Hall, Notre Dame, IN 46556, USA. [2]Thermochemistry Facility and Nanomaterials in the Environment, Agriculture, and Technology Organized Research Unit, University of California at Davis, 1 Shields Avenue, Davis, CA 95616, USA.

*To whom correspondence should be addressed. E-mail: pburns@nd.edu